

# Conformation and Electronic Population Transfer in Membrane-Supported Self-Assembled Porphyrin Dimers by 2D Fluorescence Spectroscopy

Alejandro Perdomo-Ortiz,<sup>‡,†</sup> Julia R. Widom,<sup>§,†</sup> Geoffrey A. Lott,<sup>‡</sup> Alán Aspuru-Guzik,<sup>‡</sup> and Andrew H. Marcus<sup>\*,§</sup>

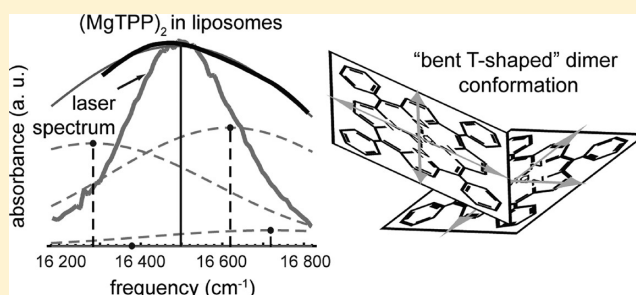
<sup>‡</sup>Department of Chemistry and Chemical Biology, Harvard University, Cambridge, Massachusetts 02138, United States

<sup>§</sup>Department of Chemistry, Oregon Center for Optics, Institute of Molecular Biology, University of Oregon, Eugene, Oregon 97403, United States

<sup>†</sup>Boise Technology, Inc., Nampa, Idaho 83687, United States

## S Supporting Information

**ABSTRACT:** Two-dimensional fluorescence spectroscopy (2D FS) is applied to determine the conformation and femtosecond electronic population transfer in a dimer of magnesium meso tetraphenylporphyrin. The dimers are prepared by self-assembly of the monomer within the amphiphilic regions of 1,2-distearoyl-*sn*-glycero-3-phosphocholine liposomes. A theoretical framework to describe 2D FS experiments is presented, and a direct comparison is made between the observables of this measurement and those of 2D electronic spectroscopy (2D ES). The sensitivity of the method to varying dimer conformation is explored. A global multi-variable fitting analysis of linear and 2D FS data indicates that the dimer adopts a “bent T-shaped” conformation. Moreover, the manifold of singly excited excitons undergoes rapid electronic dephasing and downhill population transfer on the time scale of ~95 fs. The open conformation of the dimer suggests that its self-assembly is favored by an increase in entropy of the local membrane environment.



## I. INTRODUCTION

The spontaneous assembly of aromatic and heteroaromatic groups into structured, noncovalent oligomers is an example of molecular “stacking” interactions, which are of central importance to the stability of macromolecular complexes such as DNA, light harvesting antennas, and viruses.<sup>1–5</sup> Complexes composed of porphyrin chromophores, in particular, are ubiquitous to biochemical processes that involve electronic charge or energy transport. For example, the chlorosomes of green sulfur bacteria contain hundreds of thousands of bacteriochlorophyll pigments, which self-assemble into ordered arrays that extend for hundreds of nanometers.<sup>6–8</sup> The remarkable efficiency with which these structures direct electronic excitation energy to photosynthetic reaction centers suggests the possibility to develop self-assembly strategies for new molecular electronics technologies.<sup>6,9,10</sup> Such approaches aim to tailor electronic properties, such as state-to-state couplings, coherence lengths, and transition rates, by controlling intermolecular conformation.

Given the direct connection between the electronic properties of a molecular complex and its architecture, experiments that simultaneously probe conformation-dependent electronic couplings and excited state dynamics can provide new insights into structure–property relationships. In this paper, we use two-

dimensional fluorescence spectroscopy (2D FS) to determine the three-dimensional spatial conformation and femtosecond population transfer dynamics of magnesium meso tetraphenylporphyrin dimers [(MgTPP)<sub>2</sub>], which self-assemble in the nonpolar region of a phospholipid bilayer membrane. It has been established that by using membranes to induce chromophore assembly, it is possible to exert a moderate level of control over structural parameters, such as the degree of oligomerization, the placement of the porphyrins within different dielectric regions of the membrane, and the interchromophore conformation.<sup>2</sup> Related membrane–porphyrin systems, including biomimetic models for mitochondrial electron transport reactions,<sup>2</sup> drug delivery vehicles for photodynamic cancer therapies,<sup>11,12</sup> and platforms for artificial light harvesting devices, have appeared in the literature.<sup>13</sup>

In such membrane–porphyrin systems, the hydrophobic MgTPP monomers enter the aliphatic region of the phospholipid bilayer, and at elevated concentration, the monomers self-assemble into dimers.<sup>14</sup> Within the membrane environment, the dimer adopts a preferred conformation, in which the exciton-coupling strength exceeds the spectral width of site energy

Received: June 15, 2012

Published: August 10, 2012



disorder. The stability of the dimer is sufficient to offset the loss of translational entropy of each monomer subunit, in addition to the disruption of favorable interactions between phospholipid acyl chains and the porphyrin macrocycles.

A central issue pertains to the nature of the dimer stability. One possibility is that dimerization is driven by the formation of favorable monomer–monomer interactions, whereas an alternative picture attributes dimer stability to an increase in entropy resulting from the release of phospholipid acyl chains from their MgTPP contacts. Although a precise determination of the thermodynamic forces of dimerization is beyond the scope of the current study, an indication of the role played by the local membrane environment can be gleaned from the relative “compactness” of the dimer conformation. For example, a relatively open structure, which does not maximize monomer–monomer surface contacts, would suggest that membrane-mediated dimer assembly is primarily entropy-driven.

Here, we present a general framework to describe how porphyrin dimer conformation and electronic population transfer can be elucidated using 2D FS. Although we focus here on one specific membrane-supported (MgTPP)<sub>2</sub> system, our approach can be similarly applied to any electronically coupled dimer–solvent system. The electronic states of adjacent MgTPP subunits couple through electronic interactions, which under conditions of moderate disorder leads to delocalization of the exciton-coupled states and splitting of the energy levels.<sup>15</sup> 2D FS is a variation of two-dimensional electronic spectroscopy (2D ES) that employs a sequence of four collinear femtosecond optical pulses to resonantly excite exciton-coupled states and that probes correlations between successive optical transitions.<sup>16</sup> The 2D FS experiment monitors fluorescence, which is proportional to the fourth-order electronically excited populations induced by the four-pulse sequence.<sup>14</sup> A phase-modulation lock-in detection scheme is used to obtain phase-sensitive spectroscopic information.<sup>17,18</sup> In contrast, the primary observable associated with 2D ES is the third-order polarization excited by three incident noncollinear pulses, which is phase-sensitively detected using a wave-vector-matched geometry. This fundamental difference between the two methods can lead to 2D spectra with very different appearances.

The remainder of this paper is organized in the following manner: In section 2, we review theoretical models to describe exciton-coupled molecular dimers, in which individual monomer sites can support either one or two degenerate electronic transitions. In section 3, we present a theoretical framework to describe 2D FS experiments that probe dimer conformation (zero population time limit) and electronic energy transport (nonzero population time). The relationship between 2D FS and 2D ES methods is established. In section 4, we discuss our experimental results and theoretical analysis for the membrane-supported (MgTPP)<sub>2</sub> dimer system. We further discuss the thermodynamic factors of membrane induced porphyrin dimer self-assembly. In section 5, we summarize our results.

## 2. MODELS FOR EXCITON-COUPLED DIMERS

Monomers of MgTPP have two equivalent perpendicular transition dipole moments contained within the plane of the porphyrin macrocycle (see Figure 1A, inset). These define the directions of degenerate  $Q_x$  and  $Q_y$  transitions between ground and lowest-lying excited states.<sup>19–22</sup> Both transition moments contribute to the collective exciton interactions in a molecular complex. To specify dimer conformations, we adopt a molecular-frame coordinate system similar to that described in refs 20 and

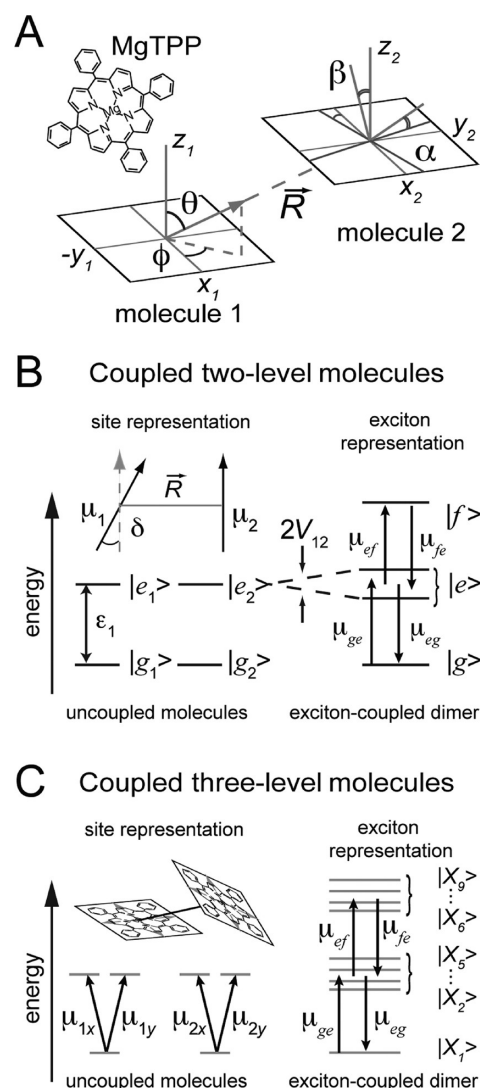


**Figure 1.** (A) Coordinate system used to describe two MgTPP monomers, whose relative conformation is defined by the molecular center-to-center vector  $\vec{R}$  and the angles  $\theta$ ,  $\phi$ ,  $\alpha$ , and  $\beta$ . (inset) Molecular formula for the MgTPP monomer. (B) Energy level diagram of two chemically identical two-level molecules. (inset) An example configuration with relative transition dipole angle  $\delta$ . Electronic interactions result in an exciton-coupled, four-level dimer with a single ground state, two singly excited states, and a single doubly excited state. Multipulse excitation can excite transitions between ground, singly excited and doubly excited state manifolds. The conformation of the dimer determines the energy level spacing and the strengths of the transitions. (C) Energy level diagram of two chemically identical three-level molecules, each with degenerate transition dipole moments directed along the  $x$  and  $y$  axes of the molecular frames. (inset) An example configuration of a (MgTPP)<sub>2</sub> dimer. Electronic interactions result in an exciton-coupled nine-level system, with a single ground state, four singly excited states, and four doubly excited states. Exciton states are labeled  $|X_1\rangle, \dots, |X_9\rangle$ .

21 and which is depicted in Figure 1A. For each monomer, a right-handed coordinate system is taken with the  $x$  and  $y$  axes lying parallel to the  $Q_x$  and  $Q_y$  transition directions, and the  $z$  axis perpendicular to the porphyrin plane. A conformation is specified by the monomer center-to-center vector  $\vec{R}$ , which is oriented relative to molecule 1 according to the polar and azimuthal angles  $\theta$  and  $\phi$ , respectively. The relative orientation of molecule 2 is given by the Euler angles  $\alpha$  and  $\beta$ . Because of the

degeneracy of the  $Q_x$  and  $Q_y$  transitions, all exciton interactions are independent of the third Euler angle  $\gamma$ , which we set to zero for all of our subsequent considerations.<sup>21</sup>

The Hamiltonian for a dimer of chemically identical  $n$ -level molecules, in which system–bath interactions are neglected, can be written

$$\hat{H} = \hat{H}^{(1)} + \hat{H}^{(2)} + \hat{V} = \hat{H}_0 + \hat{V} \quad (2.1)$$

where  $\hat{H}^{(1)}$  [ $\hat{H}^{(2)}$ ] is the Hamiltonian associated with monomer 1 (monomer 2). Within the point–dipole approximation, the electronic coupling can be expressed as

$$\hat{V} = \frac{1}{4\pi\epsilon_0 R^3} \hat{\mu}_1 \cdot \left(1 - 3 \frac{\mathbf{R}\mathbf{R}}{R^2}\right) \cdot \hat{\mu}_2 \quad (2.2)$$

where  $\mathbf{R}$  is the intermonomer center-to-center vector,  $\hat{\mu}_1$  ( $\hat{\mu}_2$ ) is the dipole operator for monomer 1 (monomer 2), and  $\epsilon_0$  is the vacuum permittivity. Although more accurate electronic coupling models can be readily implemented, the point–dipole approximation is a useful starting point for our calculations.

**A. Dimer of Two-Level Molecules (Coupled Two-Dipole Model).** We first consider the simplest case in which each monomer subunit supports a single electronic transition with energy  $\epsilon_1$ . In Figure 1B, (inset), we illustrate two transition dipole moments,  $\mu_1$  and  $\mu_2$ , with relative angle  $\delta$ . In the exciton representation, the effect of the electronic coupling is to create a four-level system consisting of a common ground state,  $|g\rangle$ ; two nondegenerate singly excited states,  $|\pm\rangle$ , with  $\epsilon_{\pm} = \epsilon_1 \pm V_{12}$  (referred to as the  $le$  state manifold); and a doubly excited state,  $|f\rangle$  with  $\epsilon_f \cong 2\epsilon_1$  (see Figure 1B). The coupling strength,  $V_{12}$ , is determined by the transition dipole moment magnitude  $|\mu|^2$  and dimer conformation according to eq 2.2 (see the Supporting Information (SI) for details). The singly excited states are related to the site basis according to  $|\pm\rangle = \{1/\sqrt{2}\} [|e\rangle|g\rangle \pm |g\rangle|e\rangle]$ . We define the tensor product states  $|ij\rangle$ , where  $i, j = g, e$ , respectively; label the states on monomer 1 and 2; and  $\{|ij\rangle\}$  is the dimer Hilbert space basis. Notice  $g$  ( $e$ ) is shorthand notation for the ground (excited) electronic state associated with each monomer. These symmetric and antisymmetric states have wave functions delocalized among the chromophore sites. The collective transition dipole moments between ground and singly excited states are given by  $\hat{\mu}_{\pm} = (1/2) [\hat{\mu}_1 \pm \hat{\mu}_2]$ , which can be written  $\hat{\mu}_{\pm} = (|\mu|/\sqrt{2}) [x(\cos \delta \pm 1) + y \sin \delta]$ , where we have taken  $\mu_1$  to be oriented along the  $x$  axis and  $\mu_2$  contained within the  $x$ – $y$  plane. Moreover, the transition dipole moments that mediate excited state absorption between singly and doubly excited states are  $\hat{\mu}_{+f} = \hat{\mu}_{+}$ , and  $\hat{\mu}_{-f} = -\hat{\mu}_{-}$ . The intensities of ground-state accessible transitions depend on the relative orientation of the dipoles in the complex. For example, an H-type configuration (i.e.,  $\uparrow\uparrow$ ) with  $\delta = 0$  results in a blue-shifted absorption spectrum, whereas a J-type configuration (i.e.,  $\rightarrow\rightarrow$ ) results in a red-shifted spectrum.<sup>15</sup> The effect of nonzero  $\delta$  is to partition intensity to the otherwise dipole forbidden transition, according to  $I_{\pm} = |\mu|^2(1 \pm \cos \delta)$ .

**B. Dimer of Three-Level Molecules (Coupled Four-Dipole Model).** For a dimer of chemically identical three-level molecules, we define the tensor product states  $\{|ij\rangle\}$ , where  $i, j = g, x, y$ , respectively, label the states on monomer 1 and 2, and  $\{|ij\rangle\}$  is the dimer Hilbert space basis. Notice  $x$  ( $y$ ) is shorthand notation for the excited electronic state associated with the  $Q_x$  ( $Q_y$ ) transition on each monomer.

We simplify our notation by denoting the nine basis states  $\{|l_i\rangle\}$ , with  $|l_1\rangle = |gg\rangle$ ,  $|l_2\rangle = |xg\rangle$ ,  $|l_3\rangle = |yg\rangle$ ,  $|l_4\rangle = |gx\rangle$ ,  $|l_5\rangle = |gy\rangle$ ,  $|l_6\rangle = |xx\rangle$ ,  $|l_7\rangle = |xy\rangle$ ,  $|l_8\rangle = |yx\rangle$ , and  $|l_9\rangle = |yy\rangle$ . On this basis, the total

Hamiltonian can be written as a nine-by-nine matrix of the form<sup>20</sup>

$$H \approx \begin{bmatrix} 0 & & & & & & & & \\ & \epsilon_1 & V_{23} & V_{24} & V_{25} & & & & \\ & V_{32} & \epsilon_1 & V_{34} & V_{35} & & & & \\ & V_{42} & V_{43} & \epsilon_1 & V_{45} & & & & \\ & V_{52} & V_{53} & V_{54} & \epsilon_1 & & & & \\ & & & & & 2\epsilon_1 & & & \\ & & & & & & 2\epsilon_1 & & \\ & & & & & & & 2\epsilon_1 & \\ & & & & & & & & 2\epsilon_1 \end{bmatrix} \quad (2.3)$$

In eq 2.3, we have assumed that  $\langle l_i | \hat{V} | l_j \rangle = 0$  for all  $l_i$ , that is, all of the diagonal contributions are associated with  $\hat{H}_0$ . To set the reference energy scale, we set  $\epsilon_g^{(i)} = 0$  with  $\hat{H}^{(i)}|g\rangle = \epsilon_g^{(i)}|g\rangle$ , and therefore,  $\hat{H}_0|gg\rangle = (\epsilon_g^{(1)} + \epsilon_g^{(2)})|gg\rangle = 0|gg\rangle$ . The value of  $\epsilon_1$  corresponds to the excitation energy associated with either the degenerate  $Q_x$  or  $Q_y$  transition of the uncoupled monomer. Then  $\hat{H}_0|l_k\rangle = \epsilon_k|l_k\rangle$  with  $\epsilon_k = \epsilon_1$  for any of the states containing one excitation ( $k = 2$ – $5$ ) and  $\epsilon_k = 2\epsilon_1$  for the states containing two excitations ( $k = 6$ – $9$ ). As we discuss below, we determined the value of  $\bar{\nu}_1 = \epsilon_1/hc = 16\,501\text{ cm}^{-1}$  from the linear absorption spectrum of uncoupled monomers suspended in liposomal membranes. Diagonalization of the Hamiltonian is straightforward, since it involves only the  $4 \times 4$  block associated with the singly excited state manifold (see Figure 1C). The eigen energies of the singly excited state manifold correspond to the exciton transitions underlying the region of interest in the experimental linear spectra. The positions and intensities of these features depend on the structural parameters of the dimer through the dependence on the couplings:

$$V_{ij} = \frac{1}{4\pi\epsilon_0 R^3} (\mu_1)_{ij} \cdot \left(1 - 3 \frac{\mathbf{R}\mathbf{R}}{R^2}\right) \cdot (\mu_2)_{ij} = \frac{\mu^2}{4\pi\epsilon_0 R^3} \kappa_{ij}^2 \quad (2.4)$$

Here, the orientation factor  $\kappa_{ij}^2$  is related to the directions of the transition dipole moments, and this vector connecting their centers according to  $\kappa_{ij}^2 = (\mu_1)_{ij} \cdot (\mu_2)_{ij} - 3[(\mu_1)_{ij} \cdot \mathbf{R}][\mathbf{R} \cdot (\mu_2)_{ij}]$ , where  $\mathbf{R} = (\sin \theta \cos \phi, \sin \theta \sin \phi, \cos \theta)$  is the monomer center-to-center unit vector, and  $(\mu_n)_{ij} = \langle l_i | \hat{\mu}_n | l_j \rangle / |\mu|$  is the normalized transition dipole moment operator. The relationship between the square of the monomer transition dipole moment and its absorption coefficient,  $\alpha$ , is given by

$$|\mu|^2 = \frac{3\epsilon_0 \hbar c}{\pi N_A} \int_{-\infty}^{\infty} d\bar{\nu} \frac{\alpha(\bar{\nu})}{\bar{\nu}} \quad (2.5)$$

In eq 2.5,  $\epsilon_0$  is the dielectric constant,  $\hbar$  is Planck's constant divided by  $2\pi$ ,  $c$  is the speed of light, and  $N_A$  is Avogadro's number. The factor  $\int_{-\infty}^{\infty} d\bar{\nu} (\alpha(\bar{\nu})/\bar{\nu})$  is the integrated optical line shape of the  $Q(0, 0)$  transition, measured in wave numbers, and divided by its frequency. We estimated this number by numerical integration of the experimental absorption line shape to be  $44.3\text{ M}^{-1}\text{ cm}^{-1}$ , which corresponds to a value of the monomer transition dipole moment of  $1.33D$ .



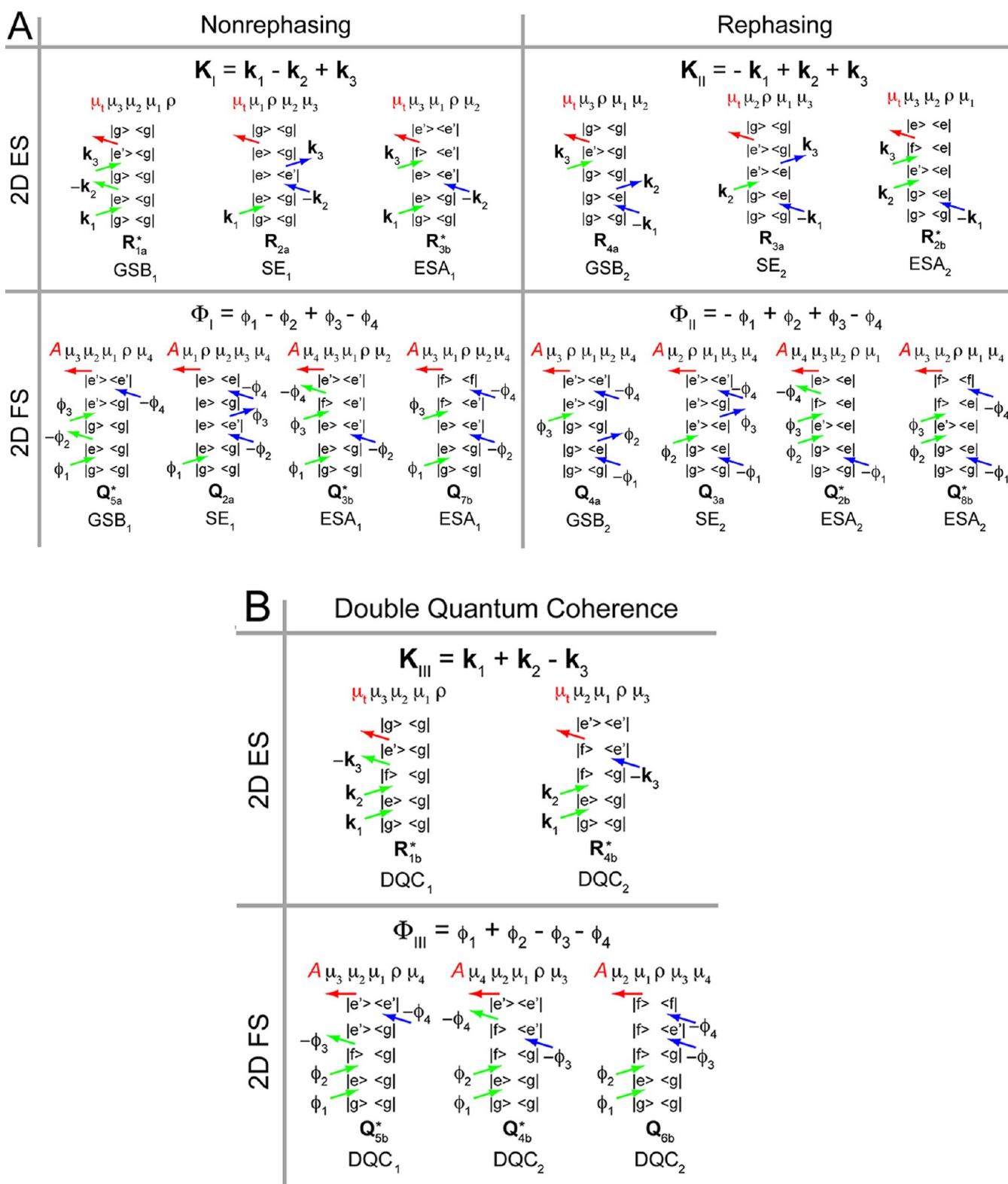


**Figure 2.** (A) DSFDs representing the light-matter interactions contributing to the rephasing and nonrephasing signals measured experimentally by 2D ES (top row) and by 2D FS (bottom row). The four- and nine-level models used to describe coupled dimers are shown in Figure 1B and C, respectively. The collective dipole moment allows transitions from the ground state to the singly excited manifold and from the latter to the final doubly excited state. The sign associated with each diagram is determined by the number of arrows (dipole interactions) on the right vertical line of each ladder diagram ("bra" side). An even (odd) number of interactions picks up a positive (negative) sign for the term under consideration. The nonrephasing and rephasing 2D ES signals are  $S_{\text{NRP}}^{2\text{D ES}}(\tau, T, t) \propto R_{1a}^* + R_{2a} - R_{3b}^*$  and  $S_{\text{RP}}^{2\text{D ES}}(\tau, T, t) \propto R_{4a}^* + R_{3a} - R_{2b}^*$ , respectively. The corresponding 2D FS signals are  $S_{\text{NRP}}^{2\text{D FS}}(\tau, T, t) \propto -(Q_{5a}^* + Q_{2a} + Q_{3b}^* - \Gamma Q_{7b})$  and  $S_{\text{RP}}^{2\text{D FS}}(\tau, T, t) \propto -(Q_{4a}^* + Q_{3a} + Q_{2b}^* - \Gamma Q_{8b})$ . The parameter  $\Gamma$  accounts for different quantum yields between doubly and singly excited state manifolds. (B) DSFDs contributing to the double quantum coherence signals measured by 2D ES (top row) and 2D FS (bottom row). The 2D ES signal is  $S_{\text{DQC}}^{2\text{D ES}}(\tau, T, t) \propto R_{1b}^* - R_{4b}^*$ , whereas the 2D FS signal is  $S_{\text{DQC}}^{2\text{D FS}}(\tau, T, t) \propto -(Q_{5b}^* + Q_{4b} - \Gamma Q_{6b})$ .

### 3. COMPARISON BETWEEN 2D FLUORESCENCE AND 2D ELECTRONIC SPECTROSCOPY

2D FS and 2D ES are conceptually similar methods, yet important distinguishing factors can result in their non-equivalence. The 2D ES signal can be interpreted as the third-order polarization of the sample, which is the source of the detected signal field. In contrast, 2D FS is a technique based on fluorescence detection.<sup>18</sup> The signal may be considered proportional to the fourth-order excited state population. We thus compare the signals of the two methods on the basis of interpretation of 2D ES signals using third-order perturbation theory, and 2D FS signals using fourth-order perturbation theory.

We consider the semiclassical light-matter interaction Hamiltonian,

$$\hat{H}_{SC} = \hat{H}_0 + \hat{H}_{int}(t), \quad \text{where } \hat{H}_{int} = -\hat{\mu} \cdot \mathbf{E}(t) \quad (3.1)$$

In 2D FS experiments, the electric field for  $P$  sequential collinear pulses polarized in the  $x$  direction can be described by  $\mathbf{E}(t) = x \sum_j^P E_j(t)$ , where the electric field of the  $j$ th pulse is given by

$$E_j(t) = \lambda_j A_j(t - t_j) \cos[\omega_j(t - t_j) + \phi_j] \quad (3.2)$$

Here,  $\lambda_j$  is the maximum intensity of the electric field,  $A_j(t - t_j) = e^{-(4\ln 2)/(\tau^2 fwhm)(t-t_j)^2}$  is the temporal envelope,  $\omega_j$  is the pulse frequency, and  $\phi_j$  is its phase. In 2D ES experiments, the noncollinear pulses are analogously described by  $E_j(t) = \lambda_j A_j(t - t_j) \cos[\omega_j(t - t_j) - \mathbf{k}_j \cdot \mathbf{r}]$ , where the phase of the  $j$ th pulse depends on its wave vector,  $\mathbf{k}_j$ .

Using the density matrix formalism, the evolution of the system is described by the Liouville–von Neumann equation

$$i\hbar \frac{\partial \hat{\rho}_I(t)}{\partial t} = [\hat{H}_{I,int}, \hat{\rho}_I(t)] \quad (3.3)$$

written in the interaction picture, such that  $\hat{O}_I(t) \equiv e^{i\hat{H}_0(t-t_0)} \hat{O} e^{-i\hat{H}_0(t-t_0)}$ . A formal solution to eq 3 is

$$\hat{\rho}_I(t) = \hat{\rho}_I(t_0) + \sum_{n=1}^{\infty} \hat{\rho}_I^{(n)}(t) \quad (3.4)$$

with

$$\begin{aligned} \hat{\rho}_I^{(n)}(t) &\equiv (-1)^n \left(\frac{i}{\hbar}\right)^n \int_{t_0}^t d\tau_n \int_{t_0}^{\tau_n} d\tau_{n-1} \cdots \\ &\int_{t_0}^{\tau_2} d\tau_1 [\hat{H}_{I,int}(\tau_n), \\ &\times [\hat{H}_{I,int}(\tau_{n-1}), [\cdots, [\hat{H}_{I,int}(\tau_1), \hat{\rho}_I(t_0)] \cdots ]]] \end{aligned} \quad (3.5)$$

The expectation of any observable,  $\langle \hat{O}(t) \rangle \equiv \text{tr}\{\hat{O}(t) \hat{\rho}(t)\} = \text{tr}\{\hat{O}_I(t) \hat{\rho}_I(t)\}$ , can be expressed as  $\langle \hat{O}_I(t) \rangle \equiv \sum_{n=0}^{\infty} \langle \hat{O}_I^{(n)}(t) \rangle$  with  $\langle \hat{O}_I^{(n)}(t) \rangle \equiv \text{tr}\{\hat{O}_I(t) \hat{\rho}_I^{(n)}(t)\}$ .

As mentioned previously, the 2D ES signal is associated with the third-order polarization

$$\mathbf{P}^{(3)}(t) \equiv \langle \hat{\mu}^{(3)}(t) \rangle \equiv \text{tr}\{\hat{\mu}_I(t) \hat{\rho}_I^{(3)}(t)\} \quad (3.6)$$

whereas the 2D FS signal is associated with the fourth-order excited state population,

$$\hat{A}^{(4)}(t) \equiv \langle \hat{A}(t) \rangle \equiv \text{tr}\{\hat{A}_I(t) \hat{\rho}_I^{(4)}(t)\} \quad (3.7)$$

with  $\hat{A} = \sum_v \Gamma_v |v\rangle\langle v|$  a projector onto all the states,  $\{|v\rangle\} = \{|e\rangle, |f\rangle\}$ , of the excited state manifold, weighted by their respective fluorescence quantum yield coefficients,  $\Gamma_v$ . Here, we assume that the fluorescence quantum yield of all the singly excited (excitonic) states are the same and equal to 1.0, that is,  $\Gamma_e = 1.0$  for all  $\{|e\rangle\}$ . If we further assume that  $\Gamma_f = \Gamma$  for all  $\{|f\rangle\}$ , then  $0 \leq \Gamma \leq 2$ . The case of  $\Gamma = 2$  corresponds to an ideal coherent case, in which two photons are emitted via the pathway  $|f\rangle \rightarrow |e\rangle \rightarrow |g\rangle$ . In a more common scenario, one expects the relative quantum yield of the doubly excited states to be significantly smaller than for the singly excited state,  $\Gamma \approx 0$ , because of the abundance of nonradiative relaxation pathways for highly excited states.

We consider the cases for which each monomer may support either one or two ground state allowed electronic transitions, as depicted in Figure 1B and C, respectively. As described in section 2 above, couplings between monomer transitions result in a multilevel Hamiltonian described in the diagonal exciton basis as a single ground state,  $|g\rangle$ ; a manifold of singly excited states,  $|e\rangle$ ; and a manifold of doubly excited states,  $|f\rangle$ . Signals for 2D ES and 2D FS experiments are expressed by expanding third- and fourth-order terms given by eqs 3.6 and 3.7, respectively. The 2D ES signals have been derived and studied for these dimer models.<sup>16,23</sup> In Figure 2A, we show double-sided Feynman diagrams (DSFDs) contributing to the nonrephasing (NRP) and rephasing (RP) signals, respectively, and in Figure 2B for the double quantum coherence (DQC) signals. In 2D ES, these signals correspond to detection in the wave-vector-matched directions  $\mathbf{K}_{NRP} = \mathbf{k}_1 - \mathbf{k}_2 + \mathbf{k}_3$ ,  $\mathbf{K}_{RP} = -\mathbf{k}_1 + \mathbf{k}_2 + \mathbf{k}_3$ , and  $\mathbf{K}_{DQC} = \mathbf{k}_1 + \mathbf{k}_2 - \mathbf{k}_3$ . Neglecting dissipation for the moment and assuming the rotating wave approximation in the impulsive limit,<sup>16</sup> one obtains for 2D ES signals the following expressions for the nonrephasing terms:

$$R_{1a}^* \propto \sum_{e,e'} [\mu_{eg} \mu_{ge} \mu_{e'g} \mu_{ge'}]_{\mathbf{e}_1 \mathbf{e}_2 \mathbf{e}_3 \mathbf{e}_4} e^{-i\omega_{eg}\tau} e^{-i\omega_{e'g}t} \quad (3.8)$$

$$R_{2a} \propto \sum_{e,e'} [\mu_{eg} \mu_{ge} \mu_{e'g} \mu_{ge'}]_{\mathbf{e}_1 \mathbf{e}_2 \mathbf{e}_3 \mathbf{e}_4} e^{-i\omega_{eg}\tau} e^{-i\omega_{e'g}T} e^{-i\omega_{eg}t} \quad (3.9)$$

and

$$R_{3b}^* \propto \sum_{e,e',f} [\mu_{eg} \mu_{ge} \mu_{fe} \mu_{ef}]_{\mathbf{e}_1 \mathbf{e}_2 \mathbf{e}_3 \mathbf{e}_4} e^{-i\omega_{eg}\tau} e^{-i\omega_{e'g}T} e^{-i\omega_{ef}t} \quad (3.10)$$

Similarly, the rephasing terms are given by

$$R_{4a} \propto \sum_{e,e'} [\mu_{ge} \mu_{eg} \mu_{ge'} \mu_{e'g}]_{\mathbf{e}_1 \mathbf{e}_2 \mathbf{e}_3 \mathbf{e}_4} e^{-i\omega_{ge}\tau} e^{-i\omega_{e'g}t} \quad (3.11)$$

$$R_{3a} \propto \sum_{e,e'} [\mu_{ge} \mu_{e'g} \mu_{eg} \mu_{ge'}]_{\mathbf{e}_1 \mathbf{e}_2 \mathbf{e}_3 \mathbf{e}_4} e^{-i\omega_{ge}\tau} e^{-i\omega_{e'g}T} e^{-i\omega_{e'g}t} \quad (3.12)$$

and

$$R_{2b}^* \propto \sum_{e,e',f} [\mu_{ge} \mu_{e'g} \mu_{fe} \mu_{ef}]_{\mathbf{e}_1 \mathbf{e}_2 \mathbf{e}_3 \mathbf{e}_4} e^{-i\omega_{ge}\tau} e^{-i\omega_{e'g}T} e^{-i\omega_{ef}t} \quad (3.13)$$

The double quantum coherence terms are given by

$$R_{1b}^* \propto \sum_{e,e',f} [\mu_{eg} \mu_{fe} \mu_{ge'} \mu_{e'f}]_{\mathbf{e}_1 \mathbf{e}_2 \mathbf{e}_3 \mathbf{e}_4} e^{-i\omega_{eg}\tau} e^{-i\omega_{fge}T} e^{-i\omega_{e'f}t} \quad (3.14)$$

and

$$R_{4b}^* \propto \sum_{e,e',f} [\mu_{eg} \mu_{fe} \mu_{ge'} \mu_{e'f}]_{\mathbf{e}_1 \mathbf{e}_2 \mathbf{e}_3 \mathbf{e}_4} e^{-i\omega_{eg}\tau} e^{-i\omega_{fge}T} e^{-i\omega_{e'f}t} \quad (3.15)$$

Here,  $e, e'$  label the states of the singly excited manifold,  $f$  labels the doubly excited states, and  $[\mu_{ab}\mu_{cd}\mu_{jk}\mu_{lm}]_{e_1e_2e_3e_4}$  denotes the three-dimensional orientational average product  $\langle(\mu_{ab}\cdot e_1)(\mu_{cd}\cdot e_2)(\mu_{jk}\cdot e_3)(\mu_{lm}\cdot e_4)\rangle$ , where  $e_i$  is the polarization of the  $i$ th pulse. We calculated the above orientation factors using established methods.<sup>23,24</sup> We note that for the coupled two-dipole model, the orientation factors are simple functions of the relative dipole angle  $\delta$  (see Figure 1B), whereas for the four-dipole model, the orientation factors depend on all of the structural angles  $\alpha, \beta, \theta$ , and  $\phi$  (see Figure 1A). In the current experiments, all laser pulses have the same polarization. In eqs 3.8–3.15, we have adopted the convention of naming the intervals between pulses  $t_2 - t_1 = \tau$ ,  $t_3 - t_2 = T$ , and  $t_4 - t_3 = t$ . For the coupled two-level molecules depicted in Figure 1B,  $e, e' \in \{+, -\}$  are the symmetric and anti-symmetric states. For the coupled three-level molecules of Figure 1C,  $e, e' \in \{X_2, X_3, X_4, X_5\}$  is the singly excited manifold after diagonalization of the  $4 \times 4$  block of the Hamiltonian in eq 2.3, and  $f \in \{X_6, X_7, X_8, X_9\}$  is the doubly excited state manifold.

For 2D FS, the signals are phase-synchronously-detected with respect to the modulated laser fields, and are separated according to  $\Phi_{\text{NRP}} = -(\phi_1 - \phi_2 + \phi_3 - \phi_4)$ ,  $\Phi_{\text{RP}} = -(-\phi_1 + \phi_2 + \phi_3 - \phi_4)$ , and  $\Phi_{\text{DQC}} = \phi_1 + \phi_2 - \phi_3 - \phi_4$ .<sup>14,18</sup> In Figure 2A are shown the 2D FS nonrephasing and rephasing DSFDs obtained from the fourth-order perturbation expansion given by eq 3.7. In Figure 2B are shown the analogous DSFDs for the double quantum coherence terms. In contrast to 2D ES, the DSFDs for 2D FS all terminate with excited population in either the  $|e\rangle$ -state or  $|f\rangle$ -state manifolds. Nevertheless, there is a direct correspondence between 2D ES and 2D FS signal terms. It is easy to see that for the case of nonrephasing contributions, the following relations hold:  $R_{1a}^* = Q_{3a}^* \equiv \text{GSB}_1$ ,  $R_{2a} = Q_{2a} \equiv \text{SE}_1$ ,  $R_{3b}^* = Q_{3b}^* \equiv \text{ESA}_1$ , and also that  $Q_{3b}^* = Q_{7b}$ . For the rephasing contributions, we have  $R_{4a} = Q_{4a} \equiv \text{GSB}_2$ ,  $R_{3a} = Q_{3a} \equiv \text{SE}_2$ ,  $R_{2b}^* = Q_{2b}^* \equiv \text{ESA}_2$ , and that  $Q_{2b}^* = Q_{8b}$ . For double quantum coherence contributions, we have  $R_{1b}^* = Q_{3b}^* \equiv \text{DQC}_1$ ,  $R_{4b}^* = Q_{4b}^* \equiv \text{DQC}_2$ , and  $Q_{4b}^* = Q_{6b}$ .

The nonrephasing, rephasing, and double quantum coherence 2D ES signals are written as

$$S_{\text{NRP}}^{2\text{DES}}(\tau, T, t) \propto R_{1a}^* + R_{2a} - R_{3b}^* \propto \text{GSB}_1 + \text{SE}_1 - \text{ESA}_1 \quad (3.16)$$

$$S_{\text{RP}}^{2\text{DES}}(\tau, T, t) \propto R_{4a} + R_{3a} - R_{2b}^* \propto \text{GSB}_2 + \text{SE}_2 - \text{ESA}_2 \quad (3.17)$$

$$S_{\text{DQC}}^{2\text{DES}}(\tau, T, t) \propto R_{1b}^* - R_{4b}^* \propto \text{DQC}_1 - \text{DQC}_2 \quad (3.18)$$

There are two key differences between 2D ES and 2D FS that lead to nonequivalence of the two methods:

- 1 Since the 2D FS experiment is based on fluorescence detection, it is important to consider the nature of the resulting excited state of the system after its interaction with the four ultrafast pulses. Consequently, we must consider the relative impact of terms ending in the doubly excited state  $|f\rangle$  to those ending in the singly excited manifold  $\{|e\rangle\}$ . Even though mathematically we have  $Q_{3b}^* = Q_{7b}$ ,  $Q_{2b}^* = Q_{8b}$ , and  $Q_{4b}^* = Q_{6b}$ , these terms do not contribute equally because the terms  $Q_{3b}^*$ ,  $Q_{2b}^*$ , and  $Q_{4b}^*$  end up in the singly excited manifold, while the terms  $Q_{7b}$ ,  $Q_{8b}$ , and  $Q_{6b}$  end up in the doubly excited state. Since the quantum yields of singly and doubly excited states are generally different, we must account for this fact when

simulating the signals. We therefore introduce the multiplicative factor  $\Gamma$  in front of the diagrams ending in a doubly excited population (see  $Q_{7b}$ ,  $Q_{8b}^*$ , and  $Q_{6b}$  in Figure 2A and B) to capture the relative quantum yield of this doubly excited state compared with the singly excited states. Because of the abundance of nonradiative relaxation pathways for highly excited states, one expects the relative quantum yield of the doubly excited states to be significantly smaller than for the singly excited states. In a fully ideal coherent case, in which two photons are emitted via the pathway  $|f\rangle \rightarrow |e\rangle \rightarrow |g\rangle$ , then  $\Gamma = 2$ . In general, we expect at least partial self-quenching of the doubly excited state for systems in contact with a thermal environment, such that  $0 \leq \Gamma \leq 2$ . As discussed further below, for the dimer studied in the current work, the value  $\Gamma = 0.31$  was obtained from a global optimization analysis that compared simulated to experimental spectra.<sup>14</sup> A visual illustration of these differences is presented in section 4, where we compare for several different conformations 2D FS spectra (with  $\Gamma = 0.31$ ) to the corresponding 2D ES spectra (with  $\Gamma = 2$ ).

- 2 The GSB, SE, ESA, and DQC terms add up differently for 2D ES and 2D FS. This is a consequence of the third-order versus fourth-order perturbation approach, respectively. This is the primary reason for the different appearances of 2D FS versus 2D ES spectra.

After accounting for the differences between the two methods addressed in points 1 and 2 above, the 2D FS signals are written as

$$S_{\text{NRP}}^{2\text{DFS}}(\tau, T, t) \propto -(Q_{5a}^* + Q_{2a} + Q_{3b}^* - \Gamma Q_{7b}) \propto -[\text{GSB}_1 + \text{SE}_1 + (1 - \Gamma) \cdot \text{ESA}_1] \quad (3.19)$$

$$S_{\text{RP}}^{2\text{DFS}}(\tau, T, t) \propto -(Q_{4a} + Q_{3a} + Q_{2b}^* - \Gamma Q_{8b}^*) \propto -[\text{GSB}_2 + \text{SE}_2 + (1 - \Gamma) \cdot \text{ESA}_2] \quad (3.20)$$

$$S_{\text{DQC}}^{2\text{DFS}}(\tau, T, t) \propto -(Q_{5b}^* + Q_{4b}^* - \Gamma Q_{6b}) \propto -[\text{DQC}_1 + (1 - \Gamma) \cdot \text{DQC}_2] \quad (3.21)$$

Although the signal expressions corresponding to the two methods are closely related, the variable sign contribution of the ESA and  $\text{DQC}_2$  terms in the 2D FS expressions (eqs 3.19–3.21), in comparison with the well-known negative sign ESA contributions and DQC relationships<sup>25</sup> in 2D ES spectroscopy (eqs 3.16–3.18), can lead to considerable differences in the appearance of 2D spectra. We emphasize that the differences in sign assignments between these terms arises from the commutator expansions of eq 3.5.

We first consider the case in which the interval between the second and third pulses, the so-called population time,  $T$ , is equal to zero. In this limit, the 2D spectral line shape should depend predominantly on the static energy level structure of the exciton-coupled dimer, with little contribution from electronic population transfer. To account for optical dephasing, inhomogeneous broadening, and other dissipative processes, we multiply each term given by eqs 3.16–3.21 by a phenomenological line-broadening function, which is assumed to be Gaussian with respect to both coherence times,  $\tau$  and  $t$ . That is, the rephasing signals are multiplied by the factors



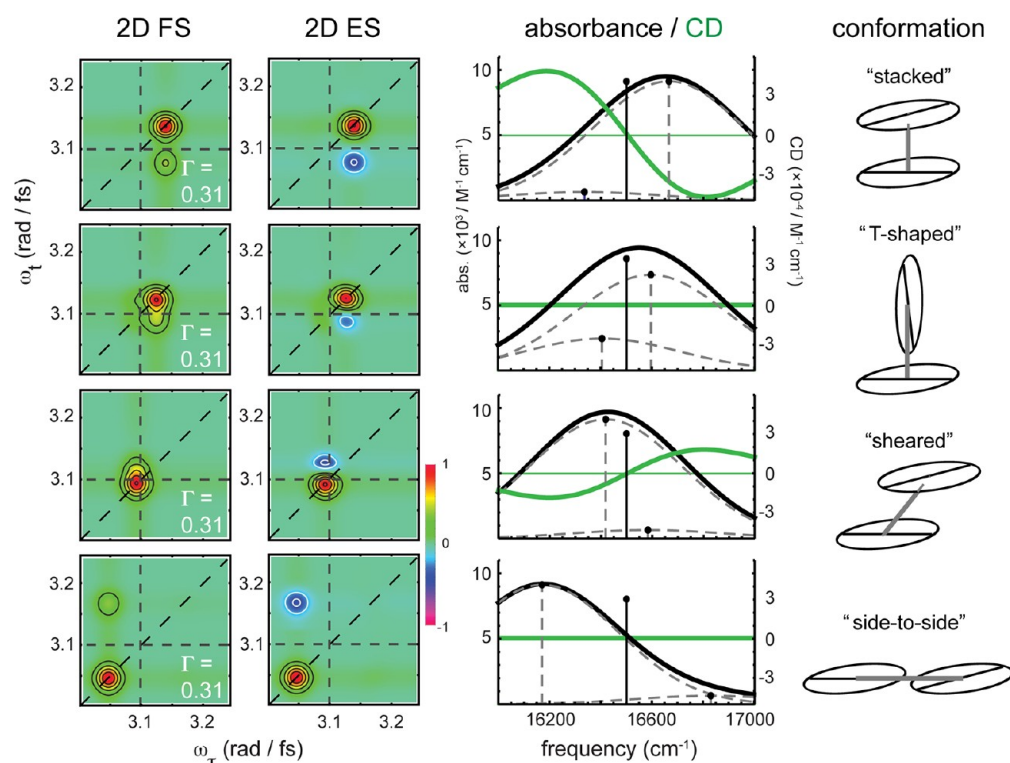


**Figure 3.** Comparison between simulated 2D FS and 2D ES total correlation spectra (real part), linear absorption, and circular dichroism (CD) using the coupled two-level model. Calculations for four selected dimer conformations are shown. Linear absorption (shown as solid black curves) and CD spectra (green curves) were calculated using standard procedures (detailed in the SI) with structural parameters  $R = 3.4 \text{ \AA}$ ,  $\delta = 30^\circ$ , and dipole moment  $\mu = 1.33D$ . Also shown are the positions of the underlying exciton features (dashed gray curves), which are evenly spaced about the monomer transition frequency  $\bar{\omega}_1 = 16501 \text{ cm}^{-1} = 3.11 \text{ rad fs}^{-1}$ . 2D spectra were calculated assuming a uniform laser spectral density, and using eqs 3.16 and 3.17 for 2D ES, and eqs 3.19 and 3.20 for 2D FS. Horizontal and vertical dashed lines indicate the monomer transition frequency.

$e^{-(\tau^2/\sigma_{\text{NRP}}^2)}$  and  $e^{-(t^2/\kappa_{\text{NRP}}^2)}$ . Similarly, we use factors containing the parameters  $\sigma_{\text{NRP}}^2$  ( $\sigma_{\text{DQC}}^2$ ) and  $\kappa_{\text{NRP}}^2$  ( $\kappa_{\text{DQC}}^2$ ) to describe the broadening of the nonrephasing (double quantum coherence) optical line shapes. Fourier transformation of these equations to the  $\omega_r$  and  $\omega_t$  domains provides the complex-valued 2D spectra  $S_{\text{NRP}}^{2\text{DFS}}(\omega_r, T, \omega_t)$  (with similar expressions for rephasing and double quantum coherence spectra). Complex-valued rephasing and nonrephasing spectra were summed to construct the total correlation spectra (TCS), according to  $S_{\text{NRP}}^{2\text{DFS}}(\omega_r, T, \omega_t) + S_{\text{RP}}^{2\text{DFS}}(\omega_r, T, \omega_t) = S_{\text{TCS}}^{2\text{DFS}}(\omega_r, T, \omega_t)$ .<sup>26</sup> The real and imaginary parts of the total correlation spectra effectively partition the absorptive and dispersive contributions to the nonlinear optical response.

In Figure 3, we present model calculations of absorbance, CD, 2D FS, and 2D ES total correlation spectra corresponding to four example conformations using the coupled two-dipole model. These calculations illustrate the sensitivity of a selected set of spectroscopic observables to, for example, different local arrangements of adjacent bases in a single strand of DNA. The figure compares adjacent "stacked," "T-shaped," "sheared," and in-line "side-to-side" conformations. For these calculations, we assumed a flat laser spectrum, and we used values for the relative dipole angle  $\delta = 30^\circ$  (with the exception of the "T-shaped" structure, for which we used  $\delta = 60^\circ$ ), interdipole separation  $R = 3.4 \text{ \AA}$ , dipolar strength  $|\mu| = 1.33D$ , and monomer transition frequency  $\epsilon_1/\hbar c = 16501 \text{ cm}^{-1}$ . For the "sheared" conformation, the angle subtending the parallel planes containing the dipoles and the interdipole vector was set to  $45^\circ$ . Exciton features underlying the absorption spectral line shapes were modeled as Gaussians, with  $\text{fwhm} = 700 \text{ cm}^{-1}$ . 2D line shapes were modeled

using a line width with  $\text{fwhm} = 175 \text{ cm}^{-1}$ . CD was calculated using standard methods,<sup>27</sup> which we briefly describe in the SI.

For the "stacked" conformation (top row), the helical H-type arrangement of transition dipoles results in a strong blue-shifted transition and a relatively weak red-shifted one. This conformation also exhibits a strong CD signal and blue-shifted diagonal peaks in the 2D FS and 2D ES spectra. The appearance of cross-peaks in the 2D FS and 2D ES spectra indicate coupling between excitons. In general, conformations that result in strong blue-shifted transitions also give rise to 2D spectral cross-peaks below the diagonal line. Conversely, conformations resulting in red-shifted spectra exhibit cross-peaks above the diagonal line. The effect of changing dimer conformation is to alter the coupling interaction  $V_{12}$ , defined in eq 2.4.

For the case of the "T-shaped" conformation (second row), the magnitude of  $V_{12}$  is diminished as a result of the larger relative angle  $\delta = 60^\circ$  between transition dipole moments. Moreover, the lack of helicity in this conformation leads to loss of the CD signal. For the helical "sheared" conformation (third row), the sign of the coupling  $V_{12}$  is inverted relative to the "stacked" conformation, which results in a shift of the primary transition strength to the lower energy exciton. This effect is accompanied by a change in sign of the CD spectrum and intense red-shifted diagonal peaks in both 2D FS and 2D ES. The "side-to-side" conformation (bottom row) results in a red-shifted pattern similar to the "sheared" structure. However, in this case, the exciton splitting is enhanced because of its greater coupling strength. The absence of helicity in the "side-by-side" conformation leads to loss of the CD signal.

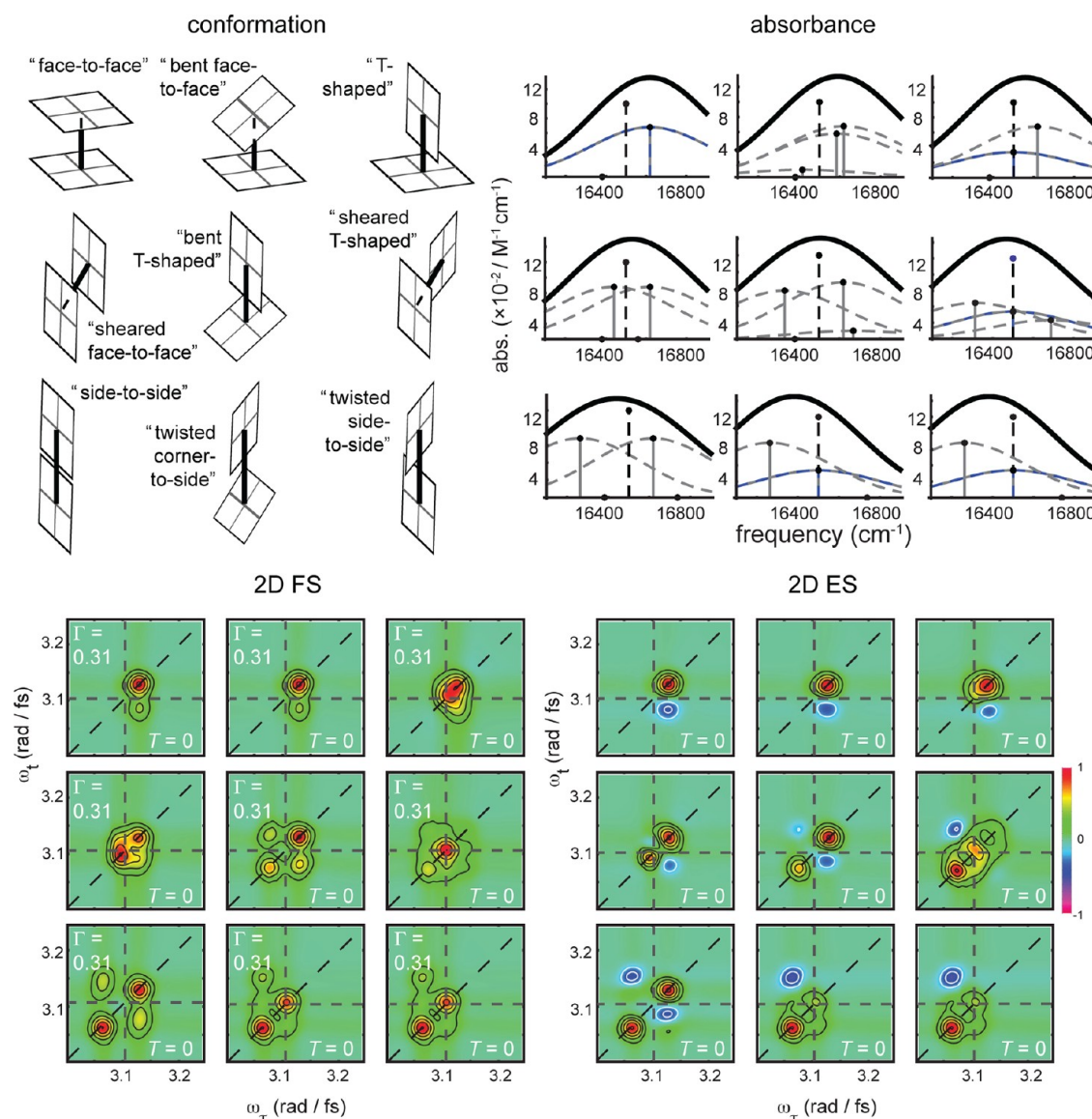


**Figure 4.** Spectroscopic and structural parameters used in these calculations were as follows. For all conformations,  $R = 4.2 \text{ \AA}$ ,  $|\mu| = 1.33\text{D}$ ,  $\epsilon_1 = 1,650 \text{ cm}^{-1}$ , linear spectral line width  $\text{fwhm} = 700 \text{ cm}^{-1}$ , 2D spectral linewidths  $\text{fwhm} \approx 170 \text{ cm}^{-1}$ . 1. face-to-face:  $\theta = \phi = \alpha = \beta = 0$ ; 2. bent face-to-face:  $\theta = \phi = \alpha = 0$ , and  $\beta = 45^\circ$ ; 3. T-shaped:  $\theta = \phi = \alpha = 0$ , and  $\beta = 90^\circ$ ; 4. sheared face-to-face:  $\theta = 45^\circ$ ,  $\phi = \alpha = \beta = 0$ ; 5. bent T-shaped:  $\theta = 90^\circ$ ,  $\phi = 0$ ,  $\alpha = 90^\circ$ , and  $\beta = 45^\circ$ ; 6. sheared T-shaped:  $\theta = 45^\circ$ ,  $\phi = \alpha = 0$ , and  $\beta = 90^\circ$ ; 7. side-to-side:  $\theta = 90^\circ$ , and  $\phi = \alpha = \beta = 0$ ; 8. twisted corner-to-side:  $\theta = 90^\circ$ ,  $\phi = \alpha = 45^\circ$ , and  $\beta = 90^\circ$ ; 9. twisted side-to-side:  $\theta = 90^\circ$ ,  $\phi = \alpha = 0$ , and  $\beta = 90^\circ$ .

For each of the conformations depicted in Figure 3, the primary difference between 2D FS and 2D ES spectra is the sign of the cross-peak. For the case of 2D FS, the cross-peak is positive, whereas for 2D ES, the cross-peak is negative. This difference arises as a result of the influence of the parameter  $\Gamma = 0.31$  for 2D FS, and  $\Gamma = 2$  for 2D ES. In the case of 2D ES, the ESA terms contribute with negative sign to the cross-peak amplitude (see eqs 3.19 and 3.20). The analogous ESA terms contribute with positive sign to the cross-peak amplitude in 2D FS. We emphasize that although it is not possible to determine a particular conformation using any one of these spectroscopic observables, the combination of absorbance, CD, and 2D FS (or alternatively, 2D ES) is in principle sufficient to distinguish between conformations.

We next consider the effects of varying dimer conformation in the context of the coupled four-dipole model. In Figure 4, we present simulated spectra for nine different achiral structures of

the exciton-coupled porphyrin dimer. Values for the structural parameters used in these calculations are given in the figure caption. The effect of coupling two dipoles from each monomer subunit is to increase the number of possible exciton-split ground-state allowed transitions to four. For many of the cases examined, the spectra exhibit degeneracies or transitions that carry no oscillator strength.

We note interesting similarities and differences predicted by the two models. For example, the "face-to-face" conformation (top left) results in linear and 2D spectra dominated by H-type coupling, which is similar to that of the "stacked" conformation in the two-dipole model. In contrast, the coplanar "side-to-side" conformation (bottom left) appears different from its two-dipole counterpart. For the four-dipole system, a combination of H-type and J-type coupling gives rise to significant blue- and red-shifted transitions, with each characterized by a unique splitting. The 2D spectrum corresponding to the "side-to-side" conformation



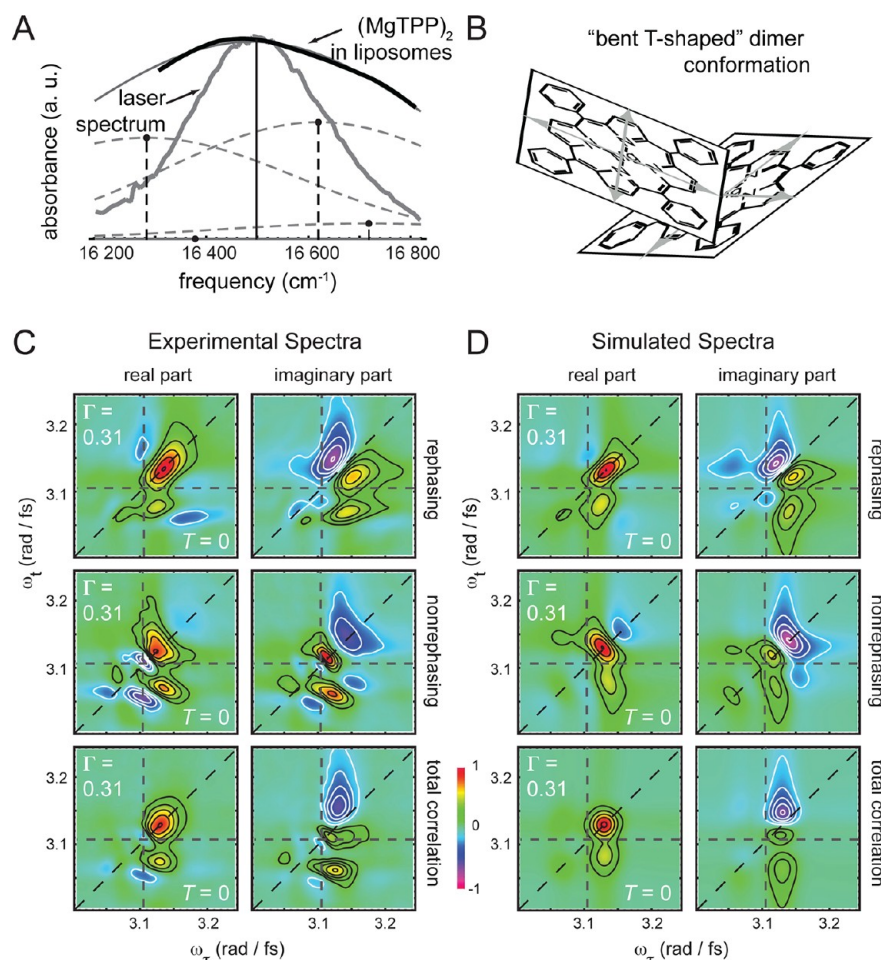


**Figure 5.** (A) Overlay of the  $(\text{MgTPP})_2$  in liposome absorbance and the laser pulse spectrum. The laser spectrum (solid gray curve) was fit to a Gaussian centered at the monomer transition frequency  $\bar{\nu}_1 = 16\,501\text{ cm}^{-1}$  (606 nm) and with  $\text{fwhm} = 327\text{ cm}^{-1}$  (12 nm). The linear absorbance (solid black curve) is compared with the simulated spectrum (solid gray curve), which is based on the “bent T-shaped” dimer conformation depicted in part B. The optimized dimer conformation corresponds to the structural parameter assignments  $R = 4.2\text{ Å}$ ,  $\theta = 117.4^\circ$ ,  $\phi = 225.2^\circ$ ,  $\alpha = 135.2^\circ$ , and  $\beta = 137.2^\circ$ . (C, D) Comparison between experimental (C) and simulated (D) rephasing (top row), nonrephasing (middle row), and total correlation (bottom row) spectra. The simulated spectra correspond to the optimized conformation depicted in part B with  $\Gamma = 0.31$ .

exhibits cross-peaks above and below the diagonal line, reflecting the two types of coupling. Similarly, both H- and J-type couplings contribute simultaneously to the spectra of the “bent T-shaped” conformation (center) and the “sheared face-to-face” conformation (middle left), although in the latter case, the coupling strengths are significantly reduced.

The effect of tilting the plane of a monomer subunit in the “face-to-face” dimer can be seen from the horizontal progression across the top row. The symmetric “T-shaped” conformation (top right) contains one pair of H-type coupled dipoles. Since the remaining dipoles of this structure are perpendicular, they do not couple, and their transition energies are unperturbed from that of the monomer. In the case of the “bent face-to-face” conformation (top middle), the two pairs of dipoles each contribute H-type coupling to the linear and 2D spectra.

The remaining three conformations—“sheared T-shaped” (middle right), “twisted corner-to-side” (bottom middle), and “twisted side-to-side” (bottom right)—share common spectroscopic characteristics. Each of these structures exhibits one pair of J-type coupled dipoles and another pair whose lack of coupling leads to transitions at the monomer frequencies. We note that the spectra of these last two conformations are identical. This is due to the high symmetry of the metallo-porphyrin molecule, which

leads to invariance of the Hamiltonian with respect to rotation of one of the monomer subunits within the plane of its macrocycle.<sup>21</sup>

The results presented in Figures 3 and 4 show that 2D FS and 2D ES are similarly sensitive to dimer conformation. As stated previously, the primary difference between the two methods is manifested in the sign of the cross-peaks of the real total correlation spectra, which are positive in the current case of 2D FS ( $\Gamma = 0.31$ ) and negative in 2D ES ( $\Gamma = 2$ ).

## 4. RESULTS AND DISCUSSION

**A. Conformation of Self-Assembled  $(\text{MgTPP})_2$  Dimer in Liposomal Membranes.** In Figure 5 are shown the results of experiments performed on  $(\text{MgTPP})_2$  samples, which were prepared in 7:1 1,2-distearoyl-*sn*-glycero-3-phosphocholine (DSPC)/MgTPP liposomes.<sup>14</sup> In these studies, a comparison was made between the line shapes of the lowest-energy electronic transitions [i.e., the  $Q(0,0)$  features] for three different samples: a solution of MgTPP in toluene, a low concentration monomer sample in liposomes (70:1 DSPC/MgTPP), and the dimer sample in liposomes. From the linear spectra, we observed that the liposomal membrane stabilizes the monomer transition energy relative to toluene. From the monomer liposome

spectrum, we determined the values of the unperturbed transition frequency,  $\bar{\nu}_1 = 16\,500.7\text{ cm}^{-1}$ , and the dipole strength,  $|\mu| = 1.33D$ . In comparison with the monomer samples, the line shape of the  $(\text{MgTPP})_2$  sample (shown in Figure 5A) was asymmetrically broadened, suggesting the presence of electronic interactions between monomer subunits that lead to splitting of the  $Q(0, 0)$  transitions. This was confirmed by 2D FS measurements of these samples, in which individual exciton-split features underlying the linear absorption line shape and associated cross-peaks were observed directly.

As described in section 2B, it is possible to model the linear absorption spectrum in terms of the structural parameters  $R$ ,  $\alpha$ , and  $\beta$  (see Figure 1A) that determine the couplings  $V_{kl}$  (eq 2.4) and the collective dipole moments, and which ultimately determine the energies and intensities of the ground-state accessible transitions. We numerically generated  $\sim 1000$  representative conformations and simulated their linear spectra. By comparing experimental and simulated data, we established that a wide distribution of  $\sim 100$  conformations could reasonably explain the linear absorption spectrum. In Figure 5A is shown the simulated linear spectrum and the four underlying component transitions of the optimized “bent T-shaped” dimer conformation (shown in Figure 5B). The linear spectrum is composed of two intense spectral features at  $16\,283$  and  $16\,619\text{ cm}^{-1}$ , one weak feature at  $16\,718\text{ cm}^{-1}$ , and one effectively dark feature at  $16\,382\text{ cm}^{-1}$ . The relatively unrestricted constraint imposed on dimer conformation by the linear spectrum is a consequence of the many possible arrangements and weights that can be assigned to the four overlapping Gaussian features with broad spectral width.

In Figure 5C are shown the complex-valued 2D FS data for the  $(\text{MgTPP})_2$  liposome sample. The 2D FS spectra depend on the overlap between the  $Q(0, 0)$  feature and the laser pulse spectrum (shown in Figure 5A). Rephasing and nonrephasing data (top and middle rows, respectively) were processed from independently detected signals according to their unique phase-matching conditions. The two types of spectra provide complementary structural information because each depends on a different set of nonlinear coherence terms. Rephasing and nonrephasing spectra were summed together to construct the total correlation spectrum (bottom row).<sup>26</sup> The 2D spectra are asymmetrically shaped, with the most prominent features a high-energy diagonal peak and a coupling peak directly below it with an apparent splitting of  $\sim 340\text{ cm}^{-1}$ . We note the similarities between the general appearance of the experimental linear and 2D spectra and between the model spectra associated with “T-shaped” and closely related dimer conformations shown in Figure 3 (for two-dipole coupled models) and in Figure 4 (for four-dipole coupled models).

By extending the procedure to simulate linear spectra, we numerically simulated the 2D spectra for a broad distribution of conformations. We performed a least-squares analysis that compared simulated and experimental spectra to obtain an optimized conformation consistent with both the 2D and linear data sets. In our optimization procedure, we treated the fluorescence efficiency,  $\Gamma$ , of doubly excited excitons as a parameter to find the value that best represents the experimental data. In Figure 5D, we directly compare our experimental and simulated 2D FS spectra for the optimized “bent T-shaped” conformation shown in Figure 5B. The values obtained for the parameters of this conformation are  $\theta = 117.4^\circ$ ,  $\phi = 225.2^\circ$ ,  $\alpha = 135.2^\circ$ ,  $\beta = 137.2^\circ$ ,  $R = 4.2\text{ Å}$ , and  $\Gamma = 0.31$ , with associated trust intervals:  $-16^\circ < \Delta\theta < 4^\circ$ ,  $-11^\circ < \Delta\phi < 11^\circ$ ,  $-11^\circ < \Delta\alpha < 11^\circ$ ,

$-2^\circ < \Delta\beta < 2^\circ$ ,  $-0.05\text{ Å} < \Delta R < 0.05\text{ Å}$ , and  $-0.1 < \Delta\Gamma < 0$ . For rephasing, nonrephasing, and total correlation spectra, the agreement between experiment and theory is very good, with an intense diagonal peak and a weaker coupling peak (below the diagonal) clearly reproduced in the simulation. A notable feature of the experimental 2D spectra is the asymmetric line shape, which is most apparent in the coupling peak. One possible explanation for these asymmetries is the existence of distinct interactions between the various exciton states and the membrane environment. The discrepancy between experimental and simulated 2D line shapes is an indication of a shortfall in the model Hamiltonian. We address this issue below in our consideration of the population time dependence of the 2D FS data. As we discuss below, this feature appears to be related to the presence of the dark transition at  $16\,382\text{ cm}^{-1}$ .

Our confidence in the conformational assignment we made was quantified by the numerical value of the regression analysis target parameter  $\chi_{\text{tot}}^2 = \chi_{\text{linear}}^2 + \chi_{2\text{D}}^2$ , which includes contributions from both linear and 2D FS spectra.<sup>14</sup> By starting with this conformation and incrementally scanning the structural parameters  $\theta$ ,  $\phi$ ,  $\alpha$ , and  $\beta$ , we observed that  $\chi_{\text{tot}}^2$  increased, indicating that the favored conformation is a local minimum when both linear and 2D spectra were included in the analysis. Similarly, we found that the value  $\Gamma = 0.31$  correspond to a local minimum. If only one of the two types of spectra is included, the restrictions placed on the dimer conformation are significantly relaxed.

**B. The Influence of Excited State Population Transfer on Time-Dependent 2D FS Spectra.** For a nonzero population time  $T$ , transfer of population between singly excited excitons can influence the 2D optical spectra of molecular aggregates.<sup>28–31</sup> Here, we examine how energy transfer processes affect 2D FS versus 2D ES experimental data.

To describe exciton population dynamics, we employed the quantum master equation in the secular approximation, which neglects the effects of short-lived coherences<sup>23</sup>

$$\frac{dG_{kj}(T)}{dt} = \sum_{l \neq k} K_{kl} G_{lj}(T) - \left( \sum_{l \neq k} K_{lk} \right) G_{kj}(T) \quad (4.1)$$

Here,  $G_{kj}(T)$  is the Green’s function probability that population is in state  $|k\rangle$  at time  $T$ , provided that state  $|j\rangle$  was originally populated at  $T = 0$ . For the coupled three-level dimer model (see Figure 1C), the indices label the singly excited excitons  $j, k, l \in \{X_2, X_3, X_4, X_5\}$ . The rate constants  $K_{kl}$  ( $K_{lk}$ ) are parameters that describe forward (backward) population transfer between pairs of states, subject to the detailed balance condition

$$\frac{K_{kl}}{K_{lk}} = e^{-(\epsilon_k - \epsilon_l)/k_B T} \quad (4.2)$$

The Green’s function solution to eq 4.1 provides time-dependent matrix elements that weight the coherence term contributions to the 2D optical spectra.<sup>23</sup> For example, if we consider a particular pair of singly excited states,  $|m\rangle$  and  $|n\rangle$  with  $\epsilon_m > \epsilon_n$ , the associated peaks and cross-peaks of the 2D total correlation function have the following forms:

$$S_{\text{TCF}}^{\text{Dm}}(\omega_r, T, \omega_l) \propto \text{GSB} + \text{SE} \cdot G_{mm}(T) + (1 - \Gamma) \cdot \text{ESA} \cdot G_{nn}(T) \quad (4.3a)$$



$$S_{\text{TCF}}^{\text{Dn}}(\omega_r, T, \omega_t) \propto \text{GSB} + \text{SE} \cdot G_{mn}(T) + (1 - \Gamma) \cdot \text{ESA} \cdot G_{mn}(T) \quad (4.3b)$$

$$S_{\text{TCF}}^{\text{Cmn}}(\omega_r, T, \omega_t) \propto \text{GSB} + \text{SE} \cdot G_{mn}(T) + (1 - \Gamma) \cdot \text{ESA} \cdot G_{mn}(T) \quad (4.3c)$$

$$S_{\text{TCF}}^{\text{Cnm}}(\omega_r, T, \omega_t) \propto \text{GSB} + \text{SE} \cdot G_{mn}(T) + (1 - \Gamma) \cdot \text{ESA} \cdot G_{mn}(T) \quad (4.3d)$$

In the above expressions, we combined nonrephasing and rephasing coherence terms (defined by eqs 3.19–3.21) to calculate the total correlation spectra, such that  $\text{GSB} = \text{GSB}_1 + \text{GSB}_2$ ,  $\text{SE} = \text{SE}_1 + \text{SE}_2$ , and  $\text{ESA} = \text{ESA}_1 + \text{ESA}_2$ . Equations 4.3a and 4.3b represent diagonal peaks (superscript *Dm*, *Dn*) at the transition frequencies of states  $|m\rangle$  and  $|n\rangle$ , respectively, and eqs 4.3c and 4.3d represent cross-peaks (*Cmn*, *Cnm*), below and above the diagonal, respectively. As described previously, in 2D FS, the parameter  $\Gamma$  is the average number of photons emitted from ESA pathways resulting in a population in doubly excited excitons relative to the number of photons emitted from ESA pathways that lead to singly excited exciton population. Self-quenching of doubly excited excitons reduces the fluorescence quantum yield such that  $0 \leq \Gamma \leq 2$ . For the  $T = 0$  data presented in Figure 5, we found the optimized value for  $\Gamma$  was 0.31.

Equations 4.3a–4.3d serve to illustrate differences between  $T$ -dependent 2D FS and 2D ES experiments. Each of the four peaks of the 2D spectrum consists of a stationary positive GSB term, a  $T$ -dependent positive SE term, and a  $T$ -dependent ESA term whose sign depends on the magnitude of  $\Gamma$ . In the case of 2D ES experiments, the ESA term has the opposite sign with respect to the SE term.

Turning to the behavior of the Green's function matrix elements, we see that downhill population transfer (i.e.,  $|n\rangle\langle nl| \rightarrow |m\rangle\langle ml|$ ) leads to a  $T$ -dependent increase in the matrix element  $G_{mn}(T)$ , and a corresponding decrease in  $G_{nm}(T)$ . Thus, the intensity of the higher-energy diagonal peak given by eq 4.3a, for example, will diminish with increasing  $T$  as a result of cancellation between a decaying positive SE term and an increasing negative ESA term. Similarly, the cross-peak given by eq 4.3c, which represents coupling from the higher to lower energy state, will increase in time because of the growth of the SE term and the decay of the ESA term. Cancellation between SE and ESA terms of opposite signs in 2D ES experiments makes these measurements sensitive to electronic population transfer. This is compared with 2D FS experiments, in which case the relative signs of SE and ESA terms need not be opposite. For  $\Gamma \leq 1$ , the factor  $(1 - \Gamma)$  that multiplies the ESA term will have the same sign as the SE term. Thus, contrast between the two terms will occur to a lesser extent. In these situations, the growth and decay of 2D FS spectral features are expected to be somewhat less sensitive to population transfer dynamics in comparison with 2D ES.

By varying the transfer rate constants defined by eqs 4.1–4.3, we simulated time-dependent 2D FS spectra, which we optimized to obtain the best agreement with our data. This procedure was accomplished using the nonlinear global optimization package KNITRO.<sup>32</sup> In our experience with other problems and this particular problem, the optimization algorithms and features of the KNITRO package allow for more robust optimization than built-in methods of computer algebra systems. In Figure 6A, we present experimental data for

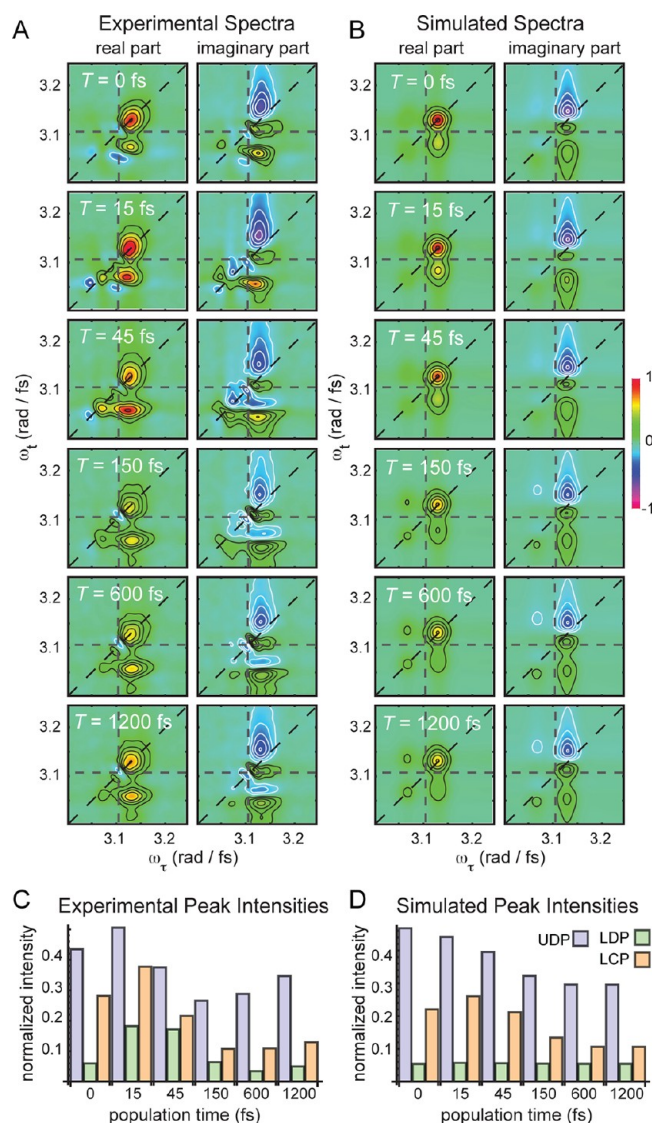


**Figure 6.** Comparison between experimental (A) and simulated (B) time-dependent 2D FS total correlation spectra of the (MgTPP)<sub>2</sub>/liposome system. Horizontal and vertical dashed lines indicate the monomer transition frequency,  $\bar{\omega}_1 = 16501 \text{ cm}^{-1} = 3.11 \text{ rad fs}^{-1}$ . The simulated spectra are based on using the optimized structural and spectroscopic parameters as input. Population transfer among singly excited excitons was modeled using a Green's function solution to the quantum master equation (see eqs 4.1–4.3) and rapid decay of the parameter  $\Gamma$  due to vibrational dephasing. (C) Time-dependent intensities of experimental 2D line shapes (UDP = upper diagonal peak, LDP = lower diagonal peak, LCP = lower cross-peak). (D) Time-dependent intensities of simulated 2D line shapes.

population times  $T = 0, 15, 45, 150, 600$ , and  $1200$  fs. These spectra were normalized to the highest intensity feature within the  $T = 0$  fs data set. We note the following general trends: At  $T = 0$  fs, there is a significantly intense peak along the diagonal centered at  $\omega_r = \omega_t \approx 16620 \text{ cm}^{-1}$ , and a cross-peak below the diagonal at  $\omega_r \approx 16620 \text{ cm}^{-1}$  and  $\omega_t \approx 16280 \text{ cm}^{-1}$ . A second, relatively weak diagonal peak is present at  $\omega_r = \omega_t \approx 16280 \text{ cm}^{-1}$ . These 2D spectral features are fully accounted for by the optimized “bent T-shaped” dimer conformation, whose linear spectrum is shown in Figure 5A. For population times  $T = 15$  and  $45$  fs, the intensities of the lower-diagonal peak and the cross-peak increase, and the intensity of the upper-diagonal peak



decreases to a minor extent. We further note the appearance at these short times of a weak diagonal peak at  $\omega_r = \omega_t \approx 16\,393\text{ cm}^{-1}$  and an associated cross-peak at  $\omega_r \approx 16\,393\text{ cm}^{-1}$  and  $\omega_t \approx 16\,280\text{ cm}^{-1}$ . Interestingly, this third feature occurs at a frequency very close to that of the dark state of the bent T-shaped dimer ( $16\,382\text{ cm}^{-1}$ ) and not far from that of the uncoupled monomer transition ( $16\,501\text{ cm}^{-1}$ ). As the population time is further increased, approaching the value  $T = 1200\text{ fs}$ , the intensities of all the observed features in the 2D spectra gradually decrease.

As discussed in section 4A, a multivariable regression analysis was implemented on the  $T = 0$  data sets to obtain the optimized structural and spectroscopic parameters.<sup>14</sup> These parameters (i.e.,  $\mathbf{R}$ ,  $\alpha$ ,  $\beta$ ,  $\Gamma$ , etc.) were used as input to our analysis of the time-dependent data. For the optimized conformation, only two of the singly excited excitons, with  $\varepsilon_{X2} = 16\,283\text{ cm}^{-1}$  and  $\varepsilon_{X4} = 16\,619\text{ cm}^{-1}$ , appear to contribute. The weaker transition at  $\varepsilon_{X5} = 16\,718\text{ cm}^{-1}$  occurs near the blue edge of the laser spectrum, and does not appear as a diagonal peak in the 2D FS spectra. The transition at  $\varepsilon_{X3} = 16\,382\text{ cm}^{-1}$  is effectively dark according to our  $T = 0$  optimization (see Figure 5A). We therefore adopted a model that included only the  $|X_2\rangle$ ,  $|X_3\rangle$ , and  $|X_4\rangle$  states. We found that because the state  $|X_3\rangle$  carries no oscillator strength, its presence has a negligible effect on the calculated spectra. Nevertheless, we included it in our calculations for completeness.

Using the simplified model described above, the population transfer rate constants were optimized using the full set of time-dependent 2D FS data shown in Figure 6A. We found that the slow decay of all experimentally observed peak intensities could be well modeled using eqs 4.1–4.3. However, the rise of the cross-peak amplitude at  $T = 15\text{ fs}$  and  $T = 45\text{ fs}$  could not be reproduced using this approach alone. We therefore consider the possibility that in addition to the population transfer mechanism described by the master equation, we must also account for the effects of fast electronic dephasing due to electron–nuclear coupling. Figure 7 illustrates the two relaxation pathways that affect the 2D FS spectra. Population is initially excited by pulses 1 and 2 within the singly excited state manifold. During the time interval  $T$ , both population transfer and rapid dephasing of electronic states coupled nuclear motion occurs. At time  $T$ , pulses 3 and 4 excite the two possible ESA pathways: the first producing population on the doubly excited state,  $|f\rangle$ , the second producing population on the singly excited state manifold,  $|e\rangle$ . Because the fluorescence quantum yield resulting from doubly excited state population ultimately depends on deactivation pathways that couple the  $|f\rangle$  state to lower-lying electronic levels, we anticipate that the extent of electronic dephasing can reduce this pathway's importance relative to those that populate  $|e\rangle$ -state levels directly. Taken in this context, we define the parameter  $\Gamma \equiv Q_{\text{ESA}}^f/Q_{\text{ESA}}^e$  as the ratio of fluorescence quantum efficiencies due to ESA pathways that produce population in the  $|f\rangle$  state to those that produce population in the  $|e\rangle$  state. We propose that the value of  $\Gamma$  can exhibit a time-dependent decay  $\Gamma = 0.31e^{-K_{\text{ed}}T}$  that reflects the fast electronic dephasing within the  $|e\rangle$ -state manifold.

Figure 6B shows the results of our optimization using as parameters the transfer rate constants  $K_{X2X3}$ ,  $K_{X2X4}$ , and  $K_{X3X4}$ , and the electronic dephasing rate constant  $K_{\text{ed}}$ . We followed standard procedures to calculate the Green's function matrix elements based on diagonalization of the rate matrix (see the SI for details).<sup>23</sup> Our nonlinear optimization included in its target function  $\chi^2$  a comparison between simulated and experimental

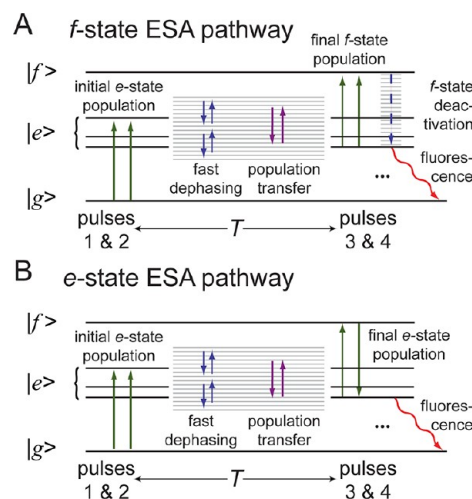


**Figure 7.** Energy level diagrams depicting the effects of population transfer and rapid electronic dephasing on excited state absorption (ESA) terms of the 2D FS signal. Pulses 1 and 2 excite initial population in the singly excited  $|e\rangle$ -state manifold, which can subsequently relax during the population period  $T$  by two primary mechanisms. These are coupling to nuclear modes and rapid electronic dephasing, in addition to downhill population transfer between electronic levels. Relaxation within the  $|e\rangle$ -state manifold is expected to have different effects on the two types of ESA pathways that contribute to 2D FS. (A) ESA signal pathways that result in population on the doubly excited  $|f\rangle$  state are susceptible to deactivation pathways, which involve coupling to nuclear coordinates. (B) ESA signal pathways that directly excite population on the  $|e\rangle$ -state manifold are expected to experience a comparatively weaker dependence on electron–nuclear coupling.

2D peak intensities for the most prominent features, the higher-energy diagonal peak (labeled  $\text{DX}_4$ ) and cross-peak ( $\text{CX}_4\text{X}_2$ ).

$$\chi^2 = \sum_T [S_{\text{TCF,exp}}^{\text{DX}_4}(T) - S_{\text{TCF,sim}}^{\text{DX}_4}(T)]^2 + [S_{\text{TCF,exp}}^{\text{CX}_4\text{X}_2}(T) - S_{\text{TCF,sim}}^{\text{CX}_4\text{X}_2}(T)]^2 \quad (4.4)$$

The values of the rate constants that minimize eq 4.4 were found to be  $K_{X2X3} = 3.6 \times 10^{-9}\text{ fs}^{-1}$ ,  $K_{X2X4} = 0.0105\text{ fs}^{-1}$ ,  $K_{X3X4} = 2.56 \times 10^{-9}\text{ fs}^{-1}$ , and  $K_{\text{ed}} = 0.86\text{ fs}^{-1}$ . By using the detailed balance condition [eq 4.2], we determined the remaining rate constants according to  $K_{X3X2} = 0.616 \times K_{X2X3} = 2.22 \times 10^{-9}\text{ fs}^{-1}$ ,  $K_{X4X2} = 0.201 \times K_{X2X4} = 2.11 \times 10^{-3}\text{ fs}^{-1}$ ,  $K_{X3X4} = 3.067 \times K_{X4X3} = 7.85 \times 10^{-9}\text{ fs}^{-1}$ ,  $K_{X2X2} = K_{X3X2} + K_{X4X2} \approx 2.11 \times 10^{-3}\text{ fs}^{-1}$ ,  $K_{X3X3} = K_{X2X3} + K_{X4X3} \approx 6.16 \times 10^{-9}\text{ fs}^{-1}$ ,  $K_{X4X4} = K_{X2X4} + K_{X3X4} \approx 0.0105\text{ fs}^{-1}$ .

This model appears to reproduce the general trends in the experimental data. Population transfer is dominated by coupling between the  $|X_2\rangle$  and  $|X_4\rangle$  states, with the downhill process occurring on the time scale  $\sim 95\text{ fs}$ , and the uphill process,  $\sim 474\text{ fs}$ . The rise of the cross-peak intensity at short population times is accounted for by electronic dephasing with time constant  $\sim 1.2\text{ fs}$ . An interesting feature observed in the experimental spectra, which the current model does not reproduce, is the appearance at short times of a weak diagonal peak at  $\omega_r = \omega_t \approx 16\,393\text{ cm}^{-1}$  and an associated cross-peak at  $\omega_r \approx 16\,393\text{ cm}^{-1}$  and  $\omega_t \approx 16\,280\text{ cm}^{-1}$ . These features could be due to greater oscillator strength in transitions to the  $|X_3\rangle$  state ( $16\,382\text{ cm}^{-1}$ ) than is allowed by the optimized structural parameters. This could be an indication that the true conformation is slightly different from the one resulting from our  $T = 0\text{ fs}$  analysis. A second possibility is that a minor

component of the MgTPP monomer is also present in the sample. This seems less likely because the monomer transition frequency ( $16\,501\text{ cm}^{-1}$ ) is further removed from the observed feature, and there is no indication of its presence in the  $T = 0\text{ fs}$  data set.

**C. Thermodynamic Considerations of Membrane Induced Porphyrin Dimer Self-Assembly.** We found that the average conformation for the  $(\text{MgTPP})_2$  dimer is a “bent T-shaped” structure with mean separation between Mg centers  $R = 3.4\text{ Å}$ . Close packing considerations alone would suggest that the most stable structure should maximize  $\pi$ – $\pi$  stacking interactions; however, entropic contributions to the free energy due to fluctuations of the amphiphilic interior of the phospholipid membrane must also be taken into account. To understand the conditions that determine dimer stability, we dissect the thermodynamic contributions to dimer assembly<sup>1</sup>.

We consider the association reaction of a dimer  $2M \rightleftharpoons M_2$  within its local membrane environment. The standard state Gibb's free energy of association  $\Delta G_{a,\text{tot}}^\circ$  can be written as the sum of contributions:

$$\Delta G_{a,\text{tot}}^\circ = \Delta G_{a,\text{M-solv}}^\circ + \Delta G_{a,\text{M-M}}^\circ + \Delta G_{a,\text{solv-solv}}^\circ \quad (4.5)$$

In eq 4.5, the first term on the right represents the contribution of monomer–solvent interactions, the second term represents monomer–monomer interactions, and the last term represents solvent–solvent interactions. The solvent–solvent term is approximated to be small, since at low monomer concentration the majority of solvent molecules do not come into contact with monomer or dimer species. The balance of enthalpic and entropic contributions to the first two terms determines the stability of the dimer. We write these, respectively, as

$$\Delta H_{a,\text{tot}}^\circ = \Delta H_{a,\text{M-solv}}^\circ + \Delta H_{a,\text{M-M}}^\circ \quad (4.6)$$

$$\Delta S_{a,\text{tot}}^\circ = \Delta S_{a,\text{M-solv}}^\circ + \Delta S_{a,\text{M-M}}^\circ \quad (4.7)$$

We next estimate the relative signs and magnitudes of the enthalpic and entropic contributions described by eqs 4.6 and 4.7. We observed that at very low concentrations of MgTPP in aqueous liposome suspensions, essentially all of the monomer is partitioned into the lipid phase, indicating favorable monomer–solvent interactions. Upon association of the dimer, fewer contacts must be formed between monomer and solvent, such that  $\Delta H_{a,\text{M-solv}}^\circ > 0$ . This factor, taken alone, should oppose dimer assembly. On the other hand, the enthalpic contribution due to forming new monomer–monomer contacts is not known. If interactions between monomers were highly favorable, this might drive dimer assembly. However, our determination of the bent T-shaped dimer conformation—a relatively open structure—suggests that the dimer does not maximize monomer–monomer surface contacts. On the basis of this observation, we infer that  $\Delta H_{a,\text{M-M}}^\circ \approx 0$ .

We next consider the entropic contributions. We expect  $\Delta S_{a,\text{M-M}}^\circ < 0$ . This term represents the entropic cost of dimer assembly, which is due to the loss of translational and rotational freedom of monomers in comparison with the dimer.<sup>5</sup> An approximate lower bound for this value, which is based on a loosely associated dimer and ignores the confining effects of the membrane, is  $\Delta S_{a,\text{M-M}}^\circ \geq -36\text{ e.u.} = -151\text{ J K}^{-1}\text{ mol}^{-1}$ . The true value is expected to be smaller in magnitude because of the reduced translational and rotational degrees of freedom of the monomer in the membrane.

Last, we consider the effect on the entropy of monomer–solvent interactions upon dimer dissociation. In the associated

state, the number of monomer–solvent contacts is expected to decrease, corresponding to an increase in the conformational freedom of the solvent. This suggests that entropic monomer–solvent interactions favors dimer assembly, such that  $\Delta S_{a,\text{M-solv}}^\circ > 0$ .

The relevant thermodynamic factors that determine dimer assembly can be summarized as follows: (1) Dimer assembly requires monomer–solvent contacts to be disrupted, resulting in a loss in enthalpic stability. (2) Condensation of the monomers to form a dimer corresponds to a loss of entropic freedom. Both factors 1 and 2 are energetic barriers to dimer assembly, which must be compensated for by a gain in conformational entropy of the local solvent environment. The balance of factors can be written as

$$T\Delta S_{a,\text{M-solv}}^\circ > (\Delta H_{a,\text{M-solv}}^\circ - T\Delta S_{a,\text{M-M}}^\circ) \quad (4.8)$$

Currently, the magnitudes of the monomer–solvent interaction terms of eq 4.8 are not known. The monomer–monomer entropy term can be accurately calculated from theory.<sup>5</sup> Knowledge of the three terms in eq 4.8 could provide insights about dimer assembly in terms of the chemical nature of the membrane–monomer interactions. One might expect temperature to be a useful control parameter. By applying a conformational analysis to temperature-dependent 2D FS measurements, it should be possible to separate enthalpic from entropic contributions to the Gibb's free energy. We have performed follow-up experiments that examine the adopted conformations of a pair of ZnTPP monomers that are chemically tethered by a flexible linker. This allows for low concentrations of the exciton-coupled chromophores to be studied over a range of temperatures without the complication of higher-order aggregate formation. The results of these experiments will be reported in a separate publication. We anticipate the energetics of “folding” of a tethered dimer to exhibit values for  $\Delta S_{a,\text{M-solv}}^\circ$  and  $\Delta H_{a,\text{M-solv}}^\circ$  nearly identical to the current system, and the value of  $\Delta S_{a,\text{M-M}}^\circ$  can be accurately determined from theory.

## 5. CONCLUSIONS

We have presented a theoretical framework for 2D fluorescence spectroscopy (2D FS) that is a highly sensitive approach to examine the conformations of electronically coupled molecular dimers in disordered complex environments. We considered two different exciton coupling models, the case of coupled two-level molecules and that of coupled three-level molecules. We demonstrated that by combining 2D FS with linear absorption or circular dichroism spectroscopy (or both), it is possible to distinguish between various different dimer conformations, including enantiomers of opposite handedness. We compared the 2D FS observables with those of 2D electronic spectroscopy (2D ES) performed by four-wave mixing. We determined that the 2D spectra measured by the two methods often appear very different because of a modification of the relative sign and magnitude of the ESA contribution in 2D FS signals. The origin of the dissimilarity is due to rapid self-quenching of the fluorescence from population on doubly excited excitons relative to the fluorescence from population on singly excited excitons.

Using a combination of 2D FS and multivariable nonlinear global analysis, we determined the conformation of spontaneously self-assembled  $(\text{MgTPP})_2$  dimers in the hydrophobic regions of phospholipid bilayer membranes at room temperature. We found that the average conformation adopted by the system is that of a “bent T-shaped” dimer. Furthermore, we

studied the time-dependence of the 2D FS total correlation spectra on time scales ranging between 15 fs and 1.2 ps. These measurements are well described using a quantum master equation to model the population transfer among singly excited exciton states and rapid electronic dephasing. The relatively “open” structure of the dimer conformation suggests that the thermodynamic factors that favor dimer assembly are closely related to the interactions of the system with the local membrane environment. Future experiments that examine the conformations of tethered dimer systems will make possible a clean separation between entropic and enthalpic contributions to the thermodynamic driving forces of membrane-induced dimer self-assembly.

## ■ ASSOCIATED CONTENT

### Supporting Information

We describe in the SI our approach to determine the magnitude of the monomer transition dipole moments and the coupling strength. We also detail in the SI the methods we employed to calculate linear absorption spectra, circular dichroism, and the Green's function matrix elements needed for our simulations of time-dependent electronic population transfer. This material is available free of charge via the Internet at <http://pubs.acs.org>.

## ■ AUTHOR INFORMATION

### Corresponding Author

\*Phone: 541-346-4809. E-mail: [ahmarcus@uoregon.edu](mailto:ahmarcus@uoregon.edu).

### Author Contributions

<sup>†</sup>These authors contributed equally to this work.

### Notes

The authors declare no competing financial interest.

## ■ ACKNOWLEDGMENTS

A.H.M. thanks Professor Tadeusz F. Molinski of the University of California at San Diego, Professor Peter H. von Hippel of the University of Oregon, and Professor Andrei Tokmakoff of the Massachusetts Institute of Technology for useful discussions. This material is based on work supported by grants from the Office of Naval Research (Grant N00014-11-1-0193 to A.H.M.) and from the National Science Foundation, Chemistry of Life Processes Program (CHE-1105272 to A.H.M.). A.P.-O. and A.A.-G. were supported as part of the Center for Excitronics, an Energy Frontier Research Center funded by the US Department of Energy, Office of Basic Sciences (DE-SC0001088).

## ■ REFERENCES

- (1) Tanford, C. *Science* **1978**, *200*, 1012–1018.
- (2) Schenning, A. P. H. J.; Hubert, D. H. W.; Feiters, M. C.; Nolte, R. J. M. *Langmuir* **1996**, *12*, 1572–1577.
- (3) McGaughey, G. B.; Gagné, M.; Rappé, A. K. *J. Biol. Chem.* **1998**, *273* (25), 15458–15463.
- (4) Steinberg, I. Z.; Scheraga, H. A. *J. Biol. Chem.* **1963**, *238* (1), 172–181.
- (5) Finkelstein, A.; Janin, J. *Protein Eng.* **1989**, *3* (1), 1–3.
- (6) Balaban, T. S. *Acc. Chem. Res.* **2005**, *38*, 612–623.
- (7) Ganapathy, S.; Oostergetel, G. T.; Wawrzyniak, P. K.; Reus, M.; Chew, A. G. M.; Buda, F.; Boekema, E. J.; Brant, D. A.; Holzwarth, A. R.; de Groot, H. J. M. *Proc. Nat. Acad. Sci.* **2009**, *106* (21), 8525–8530.
- (8) Didraga, C.; Knoester, J. *J. Luminesc.* **2003**, *102–103*, 60–66.
- (9) Wasielewski, M. *Acc. Chem. Res.* **2009**, *42* (12), 1910–1921.
- (10) Wasielewski, M. *J. Org. Chem.* **2006**, *71* (14), 5051–5066.
- (11) Moreira, L. M.; dos Santos, F. V.; Lyon, J. P.; Maftoun-Costa, M.; Pacheco-Soares, C.; Soares da Silva, N. *Aust. J. Chem.* **2008**, *61*, 741–754.
- (12) Hidalgo, A. A.; Tabak, M.; Oliverira, O. N., Jr. *Chem. Phys. Lipids* **2005**, *134*, 97–108.
- (13) Komatsu, T.; Moritake, M.; Tsuchida, E. *Chem.—Eur. J.* **2003**, *9*, 4626–4633.
- (14) Lott, G. A.; Perdomo-Ortiz, A.; Utterback, J. K.; Widom, J. R.; Aspuru-Guzik, A.; Marcus, A. H. *Proc. Nat. Acad. Sci.* **2011**, *108*, 16521–16526.
- (15) Kasha, M.; Rawls, H. R.; El-Bayoumi, M. A. *Pure Appl. Chem.* **1965**, *11*, 371–392.
- (16) Mukamel, S. *Principles of Nonlinear Optical Spectroscopy*; Oxford University Press: Oxford, 1995.
- (17) Tekavec, P. F.; Dyke, T. R.; Lott, G. A.; Marcus, A. H. *J. Chem. Phys.* **2006**, *125*, 194303–1–19.
- (18) Tekavec, P. F.; Lott, G. A.; Marcus, A. H. *J. Chem. Phys.* **2007**, *127*, 214307.
- (19) Gouterman, M. Optical Spectra and Electronic Structure of Porphyrins and Related Rings. In *The Porphyrins: Physical Chemistry, Part A*; Dolphin, D., Ed.; Academic Press: New York, 1979; Vol. III, pp 1–156.
- (20) Stomphorst, R. G.; Koehorst, R. B. M.; van der Zwan, G.; Benthem, B.; Schaafsma, T. J. *J. Porphyrins Phthalocyanines* **1999**, *3*, 346–354.
- (21) Koolhaas, M. H. C.; van der Zwan, G.; van Mourik, F.; van Grondelle, R. *Biophys. J.* **1997**, *72*, 1828–1841.
- (22) Won, Y.; Friesner, R. A.; Johnson, M. R.; Sessler, J. L. *Photosynth. Res.* **1989**, *22* (3), 201–210.
- (23) Cho, M. *Two-Dimensional Optical Spectroscopy*, 1st ed.; CRC Press: Boca Raton, 2009.
- (24) Golonzka, O.; Tokmakoff, A. *J. Chem. Phys.* **2001**, *115*, 297–309.
- (25) Kim, J.; Mukamel, S.; Scholes, G. D. *Acc. Chem. Res.* **2009**, *42* (9), 1375–1384.
- (26) Khalil, M.; Demirdoven, N.; Tokmakoff, A. *J. Phys. Chem. A* **2003**, *107* (27), 5258–5279.
- (27) Nordén, B.; Rodger, A.; Dafforn, T. *Linear Dichroism and Circular Dichroism: A Textbook on Polarized-Light Spectroscopy*; RSC Publishing: Cambridge, UK, 2010.
- (28) Mukamel, S. *Annu. Rev. Phys. Chem.* **2000**, *51*, 691–729.
- (29) Cho, M.; Fleming, G. R. *J. Chem. Phys.* **2005**, *123*, 114506.
- (30) Milota, F.; Sperling, J.; Nemeth, A.; Mančal, T.; Kauffmann, H. F. *Acc. Chem. Res.* **2009**, *42* (9), 1364–1374.
- (31) Milota, F.; Sperling, J.; Nemeth, A.; Abramavicius, D.; Mukamel, S.; Kauffmann, H. F. *J. Chem. Phys.* **2009**, *131*, 054510–054523.
- (32) Byrd, R. H.; Nocedal, J.; Waltz, R. A. *KNITRO: An integrated package for nonlinear optimization*. In *Large-Scale Nonlinear Optimization*; di Pillo, G., Roma, M., Eds.; Springer-Verlag: New York, 2006; pp 35–59.